# Crystal Engineering of Naphthalenediimide-Based Metal–Organic Frameworks: Structure-Dependent Lithium Storage

Bingbing Tian,[†,‡] Guo-Hong Ning,[‡] Qiang Gao,[†,‡] Li-Min Tan,[‡] Wei Tang,[‡] Zhongxin Chen,[‡] Chenliang Su,[†,‡] and Kian Ping Loh*,[†,‡]
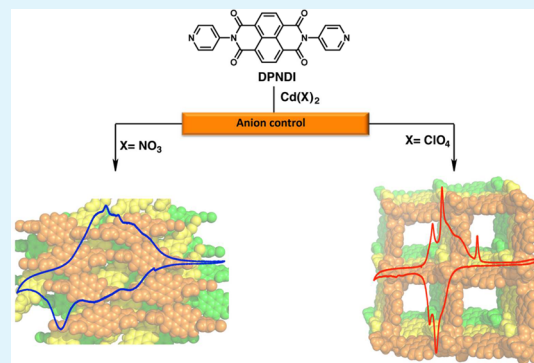
[†]SZU-NUS Collaborative Innovation Center for Optoelectronic Science & Technology, Key Laboratory of Optoelectronic Devices and Systems of Ministry of Education and Guangdong Province, College of Optoelectronic Engineering, Shenzhen University, Shenzhen 518060, China

[‡]Department of Chemistry, Centre for Advanced 2D Materials (CA2DM), Graphene Research Centre, National University of Singapore, 3 Science Drive 3, Singapore 117543

Ⓢ *Supporting Information*

**ABSTRACT:** Metal–organic frameworks (MOFs) possess great structural diversity because of the flexible design of linker groups and metal nodes. The structure–property correlation has been extensively investigated in areas like chiral catalysis, gas storage and absorption, water purification, energy storage, etc. However, the use of MOFs in lithium storage is hampered by stability issues, and how its porosity helps with battery performance is not well understood. Herein, through anion and thermodynamic control, we design a series of naphthalenediimide-based MOFs **1–4** that can be used for cathode materials in lithium-ion batteries (LIBs). Complexation of the $N,N'$-di(4-pyridyl)-1,4,5,8-naphthalenediimide (DPNDI) ligand and $CdX_2$ (X = $NO_3^-$ or $ClO_4^-$) produces complexes MOFs **1** and **2** with a one-dimensional (1D) nonporous network and a porous, noninterpenetrated two-dimensional (2D) square-grid structure, respectively. With the DPNDI ligand and $Co(NCS)_2$, a porous 1D MOF **3** as a kinetic product is obtained, while a nonporous, noninterpenetrated 2D square-grid structure MOF **4** as a thermodynamic product is formed. The performance of LIBs is largely affected by the stability and porosity of these MOFs. For instance, the initial charge–discharge curves of MOFs **1** and **2** show a specific capacity of ~47 mA h g$^{-1}$ with a capacity retention ratio of >70% during 50 cycles at 100 mA g$^{-1}$, which is much better than that of MOFs **3** and **4**. The better performances are assigned to the higher stability of Cd(II) MOFs compared to that of Co(II) MOFs during the electrochemical process, according to X-ray diffraction analysis. In addition, despite having the same Cd(II) node in the framework, MOF **2** exhibits a lithium-ion diffusion coefficient ($D_{Li}$) larger than that of MOF **1** because of its higher porosity. X-ray photoelectron spectroscopy and Fourier transform infrared analysis indicate that metal nodes in these MOFs remain intact and only the DPNDI ligand undergoes the revisible redox reaction during the lithiation–delithiation process.

**KEYWORDS:** metal–organic frameworks, crystal engineering, structural features, lithium-ion batteries, cathode materials, lithium-ion diffusion coefficient ($D_{Li}$)

## 1. INTRODUCTION

The lithium-ion battery (LIB) has established itself as one of the most successful battery technologies because of its high energy density, high rate performance, and long life span.[1–8] Transition metal oxides such as layered $LiMO_2$ (M = Co, Ni, Mn, etc.), spinel $LiM_2O_4$ (M = Mn, etc.), and olivine $LiMPO_4$ (M = Fe, Mn, Ni, Co, etc.) are conventionally used in LIBs as active cathode materials.[9–19] Recently, as a substitute material for transition metal oxides, organic-based positive electrode materials, in particular organic small molecules or polymers with redox active functional groups, have also been widely investigated because of their high theoretical specific capacities, flexibility, environmental friendliness, and sustainability.[3,20–24]

Metal–organic frameworks (MOFs) composed of an organic building block and a metal node have attracted extensive attention for their wide applications, including gas storage and separation,[25–30] catalysis,[31–34] molecule recognition,[35–39] and luminescent materials.[40,41] For a long time, people believed the MOFs are not suitable for utilization in reversible lithium storage because of their insulating nature and propensity to be structurally deformed during electrochemical cycling. For instance, Li et al. first investigated the usage of "MOF-117" [$Zn_4O(1,3,5-benzenetribenzoate)_2$] as anodes for lithium
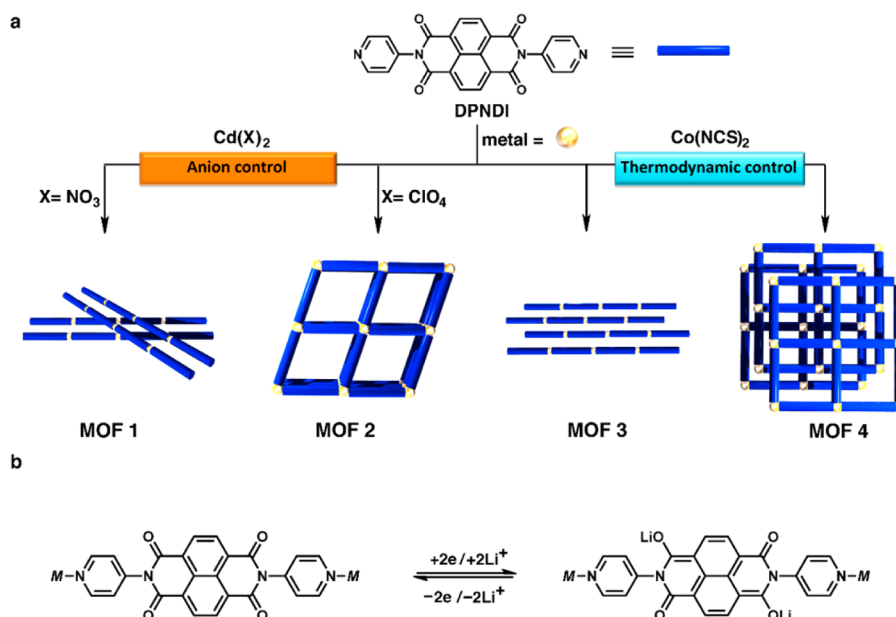
**Figure 1.** (a) Conceptual schematic presentation of crystal engineering of naphthalenediimide-based MOFs **1−4**. (b) Redox reaction of DPNDI in the MOFs. Each DPNDI unit is able to undergo two reversible one-electron redox processes.

storage and found that it presented a relatively high irreversible capacity in the first discharge cycle and a much lower reversible charge−discharge capacity in the following cycles because of the decomposition of "MOF-117" in the electrochemical process.[42] Férey and Tarascon reported the first successful example of MOF-based electrode materials for application in LIBs; "Fe-MIL-53" $\{[M^{III}OH(bdc)]$ (bdc = 1,4-benzenedicarboxylate)$\}$ was used as a positive electrode in LIBs and showed a reversible capacity of 70 mA h g$^{-1}$ within a voltage window of 1.5−3.5 V (vs Li/Li$^+$).[43] Since then, further studies have shown that MOFs have great potential as electrode materials for application in lithium storage or rechargeable LIBs.[44−46] Yoshikaw and Awaga argued that the lack of permanent porosity restricted the practical capacity of "Fe-MIL-53" in LIBs.[47] However, an understanding of how structure, i.e., stability and porosity, affects the performance of LIBs is still elusive because of the difficulty in designing and preparing isostructural MOFs. Herein, we have rationally designed a series of naphthalenediimide (NDI)-based MOFs **1−4** that allows us to probe the structure−property relationship more clearly. The mixture of the N,N'-di(4-pyridyl)-1,4,5,8-naphthalenediimide (DPNDI) ligand and CdX$_2$ (X = NO$_3^-$ or ClO$_4^-$) led to the formation of MOFs **1** and **2** with a one-dimensional (1D) nonporous network and a porous, noninterpenetrated two-dimensional (2D) square-grid structure, respectively. With the DPNDI ligand and Co(NCS)$_2$, we obtained a porous 1D MOF **3** as kinetic product, while a nonporous, noninterpenetrated 2D square-grid structure MOF **4** as the thermodynamic product was formed (Figure 1a). Compound MOFs **1** and **3** are a pair of 1D isostructural MOFs, and MOFs **2** and **4** are a pair of 2D isostructural MOFs with different porosities. We found that Cd(II) MOFs (MOFs **1** and **2**) show electrochemical stability and reversibility much higher than those of Co(II) MOFs (MOFs **3** and **4**). Consequently, when used as cathode materials in LIBs, Cd(II) MOFs (MOFs **1** and **2**) exhibit a capacity much higher than and cycling stability better than those of Co(II) MOFs (MOFs **3** and **4**). Furthermore, because of the large porosity of complex MOF **2**,

it exhibits a lithium-ion diffusion coefficient ($D_{Li}$) much higher than that of nonporous complex MOF **1**.

## 2. EXPERIMENTAL SECTION

**Materials and Methods.** The ligand DPNDI (Figure 1) was prepared according to a protocol described in the literature.[48] All the reagents and solvents for synthesis are commercially available and were used without further purification. Spectra recorded via Fourier transform infrared spectroscopy (FTIR) were recorded on an OPUS/IR PS15 spectrometer (Bruker) using KBr pellets (4000−400 cm$^{-1}$). Elemental analysis of C, H, and N was performed on an Elementar Vario Micro Cube analyzer.

**Synthesis of MOFs 1−4.** *{[Cd(NO$_3$)$_2$(DPNDI)]·(DMA)$_2$·(H$_2$O)$_{0.5}$}$_n$ (MOF 1).* A solution of Cd(NO$_3$)$_2$·(H$_2$O)$_4$ (0.02 mmol, 6.2 mg) in 1 mL of MeOH was mixed with a solution of DPNDI (0.04 mmol, 16.8 mg) in an N,N'-dimethyl acetamide (DMA)/dichlorobenzene (DCB) mixture [4/1 (v/v), 5 mL] in a glass vial. After that, the diethyl ether was slowly diffused into the resulting mixture at room temperature (rt) for 3 days. The pink rod crystals were collected by filtration and washed with Et$_2$O [yield of 49.1% based on Cd(NO$_3$)$_2$·(H$_2$O)$_4$]. IR (KBr): 3429 (br), 2395 (m), 1715 (s, C=O), 1682 (s), 1605 (s), 1576 (s), 1506 (s), 1385 (s), 1331 (s), 1246 (s), 1184 (s), 1117 (s), 1014 (s), 982 (m), 882 (m), 826 (m), 764 (m) cm$^{-1}$. Elemental analysis. Calcd for $\{(C_{24}H_{12}N_4O_4)[Cd(NO_3)_2]·(C_4H_9NO)_2(H_2O)_{0.5}\}_n$: C, 45.75; H, 3.72; N, 13.34. Found: C, 45.85; H, 3.72; N, 13.45.

*{[Cd(ClO$_4$)$_2$(DPNDI)$_2$]·(DMA)$_{4.5}$·(H$_2$O)$_2$}$_n$ (MOF 2).* The synthetic procedure for **2** was similar to that described for MOF **1**, except that a solution of Cd(ClO$_4$)$_2$·(H$_2$O)$_6$ (0.02 mmol, 8.4 mg) in 0.5 mL of MeOH was used instead of Cd(NO$_3$)$_2$·(H$_2$O)$_4$. The pale red crystals were collected by filtration and washed with Et$_2$O (yield of 31.7% based on DPNDI). IR (KBr): 3412 (br), 1715 (s, C=O), 1682 (s), 1603 (m), 1576 (s), 1506 (m), 1421 (m), 1335 (s), 1248 (s), 1188 (m), 1131 (s), 1089 (m), 1015 (m), 984 (m), 861 (m), 764 (m) cm$^{-1}$. Elemental analysis. Calcd for $\{(C_{24}H_{12}N_4O_4)_2[Cd(ClO_4)_2]·(C_4H_9NO)_{4.5}(H_2O)_2\}_n$: C, 50.17; H, 4.37; N, 11.08. Found: C, 50.44; H, 4.58; N, 10.93.

*{[Co(NCS)$_2$(DPNDI)]·(DMA)$_3$·(H$_2$O)}$_n$ (MOF 3).* A solution of Co(NCS)$_2$ (0.04 mmol, 7.0 mg) in 1 mL of MeOH was added to a solution of DPNDI (0.08 mmol, 33.6 mg) in a DMA/DCB mixture [4/1 (v/v), 5 mL] in a glass vial. After standing at rt for ~1 week, the pale red rod crystals were collected by filtration and washed with Et$_2$O

**Table 1. Crystal Data and Structural Refinement of Compound MOFs 1−4**

|  | MOF **1** | MOF **2** | MOF **3** | MOF **4** |
|---|---|---|---|---|
| crystal system | monoclinic | monoclinic | triclinic | monoclinic |
| space group | $P2_1/c$ | $C2/c$ | $P\bar{1}$ | $C2/m$ |
| $a$ (Å) | 12.3944(4) | 18.6312(5) | 7.7912(4) | 15.2849(9) |
| $b$ (Å) | 17.5823(5) | 27.1732(7) | 10.5940(5) | 19.7748(12) |
| $c$ (Å) | 16.1619(5) | 17.6238(4) | 14.2019(6) | 10.2417(7) |
| $\alpha$ (deg) | 90 | 90 | 96.488(2) | 90 |
| $\beta$ (deg) | 105.1070(10) | 108.6590(10) | 98.255(2) | 99.817(3) |
| $\gamma$ (deg) | 90 | 90 | 92.273(2) | 90 |
| $V$ (Å$^3$) | 3400.32(18) | 8453.4(4) | 1150.79(9) | 3050.3(3) |
| $Z$ | 4 | 4 | 1 | 2 |
| $D_{calcd}$ (g cm$^{-3}$) | 1.623 | 1.286 | 1.362 | 1.106 |
| $\mu$ (mm$^{-1}$) | 0.719 | 0.395 | 0.525 | 0.401 |
| $F(000)$ | 1688 | 3379.46 | 493 | 1034 |
| no. of parameters | 506 | 504 | 305 | 212 |
| $R_{int}$ | 0.0411 | 0.0430 | 0.0310 | 0.0343 |
| $R_1{}^a$ [$I > 2\sigma(I)$] | 0.0410 | 0.0569 | 0.0452 | 0.0638 |
| $R_w{}^b$ [$I > 2\sigma(I)$] | 0.1119 | 0.1743 | 0.1453 | 0.1943 |
| goodness of fit (GOF)$^c$ | 1.030 | 1.436 | 1.232 | 1.373 |

$^a R = \sum \|F_o| - |F_c\| / \sum |F_o|$. $^b R_w = \{\sum [w(F_o{}^2 - F_c{}^2)^2] / \sum w(F_o{}^2)^2\}^{1/2}$. $^c$GOF $= \{\sum [w(F_o{}^2 - F_c{}^2)^2] / (n - p)\}^{1/2}$.

[yield of 65.1% based on Co(NCS)$_2$]. IR (KBr): 3416 (br), 2120 (s), 2081 (s, SCN), 1717 (s, C=O), 1678 (s), 1607 (m), 1582 (s), 1508 (m), 1445 (m), 1421 (m), 1349 (s), 1251 (s), 1196 (m), 1149 (s), 1067 (m), 1015 (m), 985 (m), 869 (m), 766 (m) cm$^{-1}$. Elemental analysis. Calcd for $\{(C_{24}H_{12}N_4O_4)[Co(NCS)_2](C_4H_9NO)_3(H_2O)\}_n$: C, 52.44; H, 4.57; N, 14.54. Found: C, 52.17; H, 4.72; N, 14.41.

$\{[Co(NCS)_2(DPNDI)_2]\cdot(DMA)\cdot(H_2O)_5\}_n$ (MOF **4**). A solution of DPNDI (0.04 mmol, 16.8 mg) in a mixture of 4 mL of DMA and 1 mL of DCB was placed at the bottom of a test tube (inner diameter of 1 cm, height of 10 cm). MeOH (1 mL) was introduced as a buffer layer for the reaction mixture. Then, a solution of Co(NCS)$_2$ (0.02 mmol, 3.5 mg) in methaol (1 mL) was carefully added, and the test tube was allowed to stand at rt for ~3 days to give a clear blue solution. After that, diethyl ether was slowly diffused into the resultant mixture for 3 days. Pale red cubic crystals were collected by filtration and washed with Et$_2$O (yield of 50.4% based on DPNDI). IR (KBr): 3408 (br), 2119 (s), 2071 (s, SCN), 1718 (s, C=O), 1679 (s), 1604 (m), 1580 (s), 1504 (m), 1445 (m), 1421 (m), 1349 (s), 1251 (s), 1196 (m), 1150 (s), 1067 (m), 1016 (m), 985 (m), 868 (m), 766 (m) cm$^{-1}$. Elemental analysis. Calcd for $\{(C_{24}H_{12}N_4O_4)_2[Co(NCS)_2]\cdot(C_4H_9NO)(H_2O)_5\}_n$: C, 54.36; H, 3.63; N, 12.91. Found: C, 54.18; H, 3.33; N, 12.92.

**Characterization of MOFs 1−4.** Single-crystal diffraction of the MOFs was performed on a Bruker D8 VENTURE diffractometer at 100 K equipped with mirror monochromated Mo K$\alpha$ radiation ($\lambda$ = 0.71073 Å) using a $\omega$-scan mode. Empirical absorption corrections were applied using SADABS. All the structures were determined by direct methods and refined by full-matrix least-squares methods on $F^2$ using SHELXL-2014, and all non-hydrogen atoms were refined anisotropically.[49,50] The hydrogen atoms were located by geometrical calculations, and their positions and thermal parameters were fixed during the structural refinement. Crystallographic data and refinement parameters are listed in Table 1. CCDC files 1484403−1484406 contain the supplementary crystallographic data of MOFs **1−4**, respectively.

The as-prepared MOFs crystals were also characterized by powder X-ray diffraction (XRD) (BRUKER D8 diffractometer with a Cu anticathode), FTIR (transmission mode, OPUS/IR PS15 spectrometer, Bruker), field-emission scanning electron microscopy (FESEM) (JEOL JSM-6701F), transmission electron microscopy (TEM) (JEOL JEM-3011), and thermogravimetric analysis (TGA) (Discovery TGA Thermogravimetric Analyzer, TA Instruments). For analyses of the electrochemical process, the MOF-based electrodes were subjected to galvanostatic charge−discharge. The cycling was stopped at selected

stages, and these cells were disassembled and the samples rinsed with dimethyl carbonate (DMC, Sigma-Aldrich) and dried with an Ar flow, before XRD, vacuum FTIR, and X-ray photoelectron spectroscopy (XPS) (Omicron EAC2000-125 analyzer, 10$^{-9}$ Torr, Al K$\alpha$ monochromatized radiation, $h\nu$ = 1486.6 eV) analyses were performed.

**Electrochemical Measurements.** CR2016-type coin cell batteries were assembled to analyze the electrochemical behaviors. MOFs **1−4** were mixed with Super P as a conductive additive and polyvinylidene fluoride (PVDF) as a binder in a 45/45/10 weight ratio in NMP and stirred overnight to form a slurry. The slurry was coated and then pressed onto an aluminum foil substrate as the electrode. The as-prepared electrode was dried at 60 °C in vacuum for more than 24 h and then cut into Φ14 mm circular electrode discs. Lithium discs were used as the anode electrodes. The electrolyte was 1 M LiPF$_6$ in a 1/1/1 (volume ratio) mixture of ethylene carbonate (EC), ethylene methyl carbonate (EMC), and dimethyl carbonate (DMC). The separator was a Whatman Glass Microfibre Filter. The cells were assembled in a glovebox filled with argon gas, and charge−discharge tests were performed in the voltage range of 1.8−3.4 V (vs Li/Li$^+$) at a current density of 100 mA g$^{-1}$ on a LANHE (Wuhan, China) battery tester. Cyclic voltammetry (CV) and electrochemical impedance spectroscopy (EIS) were performed on an Ivium-n-Stat multichannel electrochemical analyzer. Cyclic voltammograms (CVs) were recorded in the potential window of 1.8−3.4 V (scanning rate of 0.1 mV s$^{-1}$), starting from OCP in the cathodic direction. EIS analysis was performed in the frequency range of 10 mHz to 100 kHz (potential perturbation of 10 mV). Before EIS measurement, the cell was kept at fixed potential for >30 min. The equilibrium of the cells was supposed to be reached when the change in voltage was <0.01 V in 10 min.

## 3. RESULTS AND DISCUSSION

**Crystal Structures of MOFs 1 and 2.** Single-crystal analysis reveals that (Figure 2a,b) the nonporous coordination polymer MOF **1** is crystallized in the monoclinic space group $P2_1/c$ and distorted pentagonal bipyramidal Cd(II) ions are linked by DPNDI ligands. Via the O atoms of a DMA molecule, two bidentate NO$_3^-$ ions satisfied the remaining five open sites of the Cd(II) ion. Both bidentate NO$_3^-$ ions take part in anion−π interactions with the imide rings of DPNDI ligands (centroid distances of 3.00 and 2.80 Å, respectively) of neighboring 1D chain frameworks (Figure 2 and Figure S1). In contrast, the ClO$_4^-$ ion in MOF **2**, unlike the NO$_3^-$ ion in
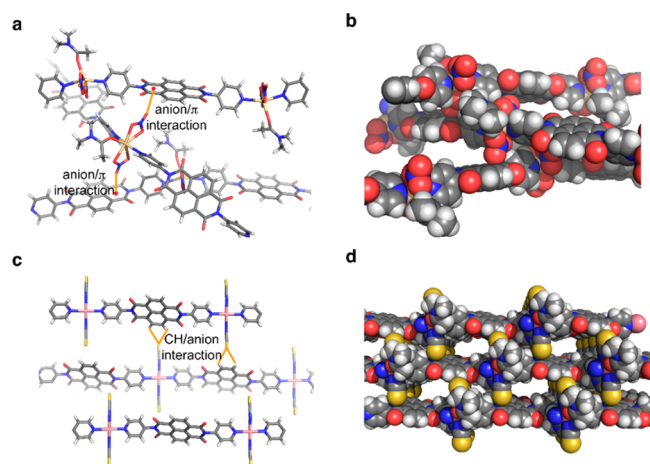
**Figure 2.** Crystal structure of the 1D chain MOF. (a) MOF **1** shows that the DPNDI ligand-linked Cd(II) ions are coordinated by two bidentate $NO_3^-$ anions, which form anion−$\pi$ interactions with the DPNDI ligand. (c) MOF **3** shows CH−anion interactions with the aromatic hydrogen in DPNDI ligands. (b) Spherical packing model of MOF **1** without porosity. (d) Spherical packing model of MOF **3** that shows the channel. In all the figures, the disordered solvent DMA molecules have been omitted for the sake of clarity (carbon, gray; oxygen, red; nitrogen, blue; sulfur, yellow; cadmium, wheat; cobalt, pink).
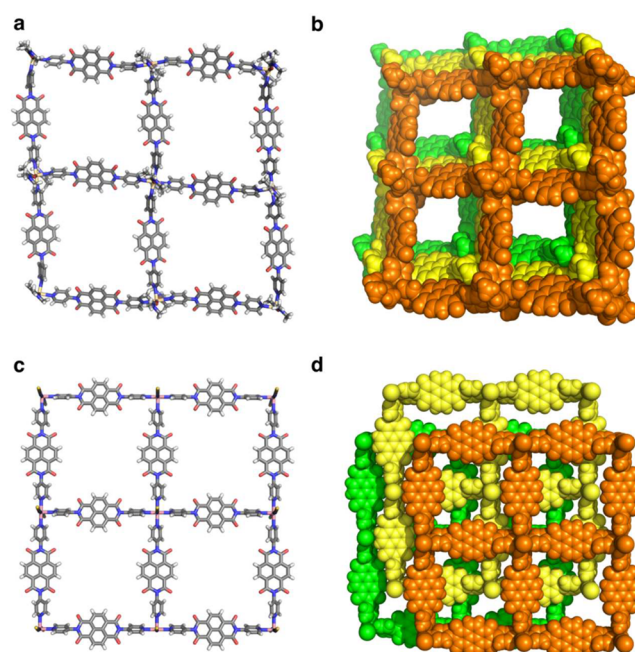


**Figure 3.** Stick models of a single layer of (a) MOF **2** and (c) MOF **4** (carbon, gray; oxygen, red; nitrogen, blue; sulfur, yellow; cadmium, wheat; cobalt, pink) and sphere models of layer stacking of the square-grid (b) MOF **1** showing the large porosity and (d) MOF **3** showing the small porosity (each layer is colored differently, i.e., orange, yellow, and green in the spherical packing model). In all the figures, the $ClO_4^-$ counterion and disorder solvent DMA molecules have been omitted for the sake of clarity.

MOF **1**, does not coordinate to the Cd(II) ion because of the weak coordination ability of the $ClO_4^-$ ion. MOF **2** possesses large noninterpenetrated square cavities (20 Å × 20 Å), and each cavity is filled with two $ClO_4^-$ ions and DMA solvent molecules, which occupy 27% of the volume of MOF **2** (Figure 3a,b). Four equatorial DPNDI ligands via the pyridyl N atom and two axial DMA molecules through the O atom are linked by octahedral Cd(II) ions, giving an array of distorted square cavities with ∠Cd−Cd−Cd values of 94.62° and 85.38°, respectively, in slipped square-grid frameworks. Importantly, the $ClO_4^-$ ions play crucial roles in prohibiting interpenetration of frameworks by partially occupying the pores; they also facilitate parallel stacking of the sheets by providing multisite CH−anion hydrogen bonding interactions ($d_{CH-O}$ values of 2.77 and 2.62 Å) with the aromatic hydrogen in the DPNDI ligands (Figure S3). In addition, the dihedral angle between pyridyl groups and the DPNDI core is ∼82°, resulting in the pyridyl groups' hydrogen (Py-Hs) being nearly perpendicular to the 2D network plane. Such an orientation allows the formation of additional CH−anion interactions ($d_{CH-O}$ values of 2.52, 2.81, 2.96, and 3.02 Å) between $ClO_4^-$ anions and Py-Hs (Figure S3). Therefore, $ClO_4^-$ ions not only occupy 1D channels but also align planar grids parallel to each other, thereby prohibiting interpenetration of frameworks.

**Crystal Structures of MOFs 3 and 4.** When the DPNDI ligand is reacted with $Co(NCS)_2$ instantly, we obtain MOF **3** as a kinetic product with a 1D chain structure similar to that of MOF **1**. Analysis of crystal structures shows that MOF **3** crystallized in the triclinic space group $P\bar{1}$ and the octahedral Co(II) ions are linked by two DPNDI ligands, two DMA molecules, and two NCS⁻ ions. It is noteworthy that the linear NCS⁻ ions assist the formation of square cavities (7 Å × 3 Å) through the CH−anion hydrogen bonding interactions ($d_{CH-O}$ values of 2.94 and 3.10 Å) with aromatic hydrogen in the DPNDI ligands of neighboring 1D chain frameworks (Figure

2c,d). The square cavities are filled with DMA molecules, which occupied 9.3% of the volume of MOF **3**.

Surprisingly, when the methanolic solution of $Co(NCS)_2$ is slowly mixed with the DPNDI ligand, MOF **4**, which is isostructural to MOF **2**, is obtained as a thermodynamic product. A 2D noninterpenetrated square-grid structure with dimensions of 19 Å × 19 Å is observed from the single crystallographic analysis. These 2D layers stack on each other to form small irregular channels (8.0% of the volume of MOF **4**), which are filled with DMA solvent molecules (Figure 3c,d). The octahedral Co(II) ions are coordinated to four equatorial DPNDI ligands and two axial NCS⁻ ions, which insert into the neighboring square cavities and interacted with the aromatic hydrogen in DPNDI ligands via multiple CH−anion hydrogen bonding interactions ($d_{CH-S}$ = 3.08 Å) (Figure S6). In addition, the linear NCS⁻ ions prevent the formation of interpenetrated structure through the anion−$\pi$ interactions with the imide rings in the DPNDI ligands (centroid distance of 3.19 Å) of separated 2D sheet frameworks (Figure S6). All the factors mentioned above contribute to the prevention of network interpenetration.

**Electrochemical Behavior of MOFs 1−4.** The discharge−charge voltage profiles of Cd(II) MOFs (MOFs **1** and **2**), Co(II) MOFs (MOFs **3** and **4**), and the DPNDI ligand at 100 mA g⁻¹ in the potential range of 1.8−3.4 V (vs Li/Li⁺) (Figure 4a−e, respectively) present the electrochemical properties of the MOFs as cathodes in LIBs. The initial discharge−charge profiles of the Cd(II) MOFs (MOFs **1** and **2**) show a similar specific capacity of ∼45 mA h g⁻¹. A sloping plateau is observed in the charge−discharge profiles of MOF **1** within the potential ranges of 2.8−2.0 V, with an output gravimetric capacity of ∼40 mA h g⁻¹, while for MOF **2**, a flatter plateau is
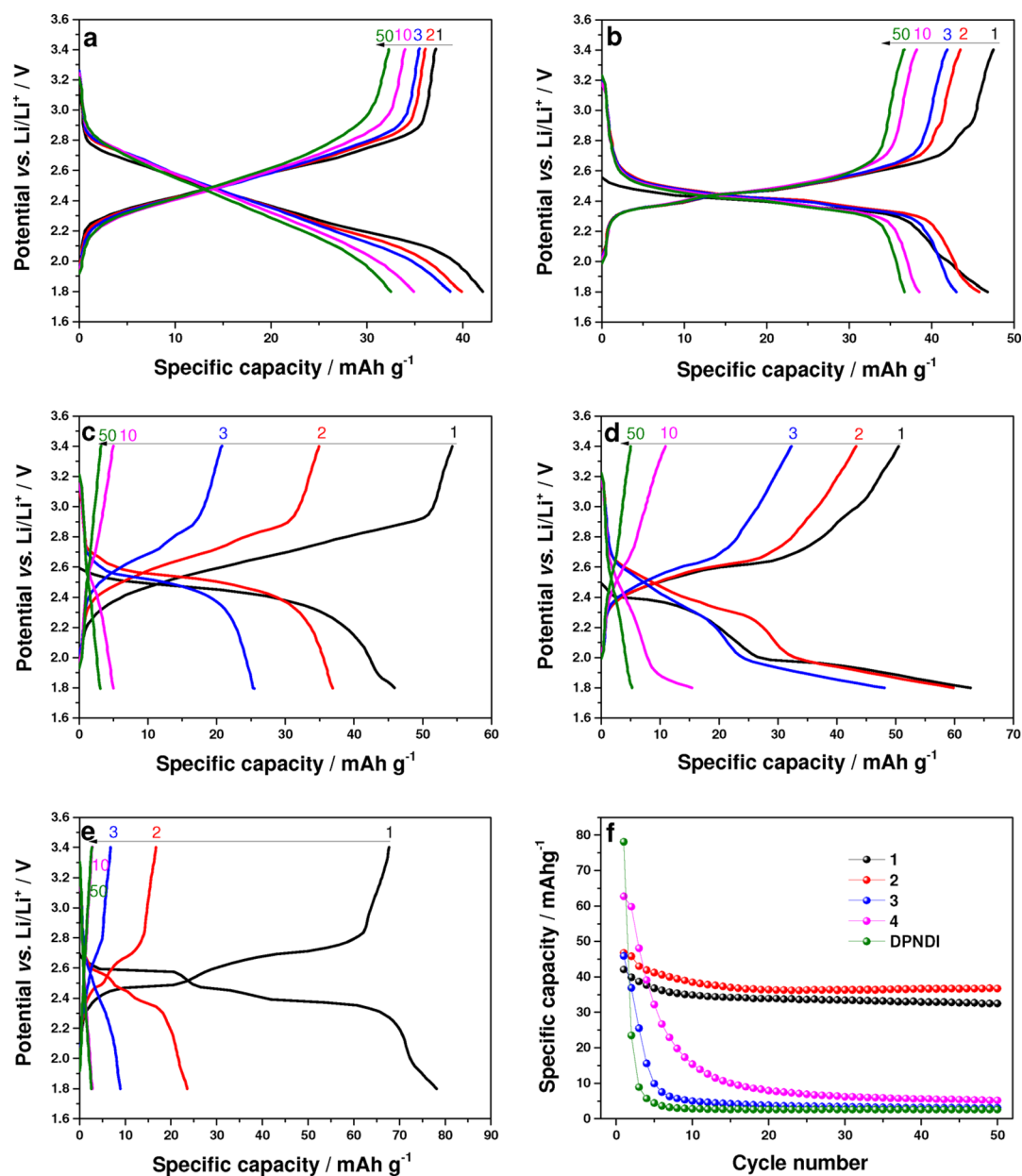
**Figure 4.** First, second, third, tenth, and fiftieth discharge−charge curves of Cd(II) MOFs [MOFs **1** (a) and **2** (b)], Co(II) MOFs [MOFs **3** (c) and **4** (d)], and the DPNDI ligand (e) at a current rate of 100 mA g$^{-1}$ in the potential range of 1.8−3.4 V. (f) Cycling performance of MOFs **1**−**4** and the DPNDI ligand.
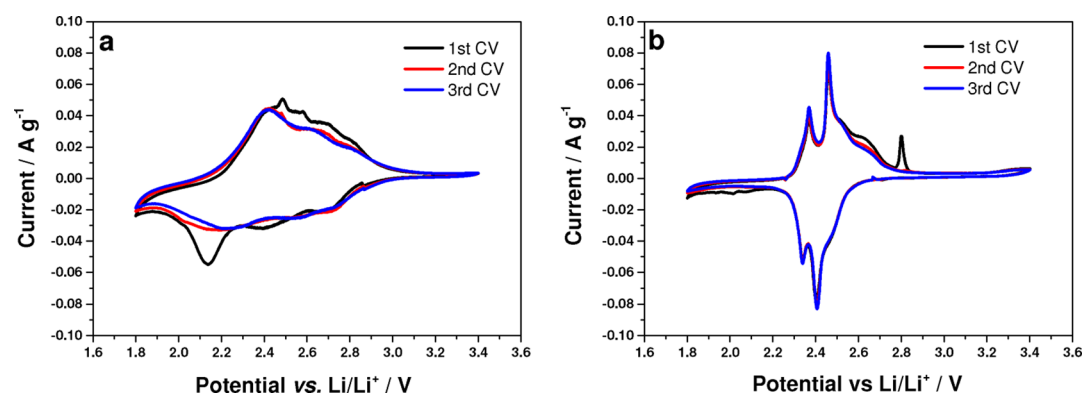


**Figure 5.** First, second, and third CV curves of Cd(II) MOFs [MOFs **1** (a) and **2** (b)]. The scan rate was 0.1 mV s$^{-1}$, and the potential range was 1.8−3.4 V.
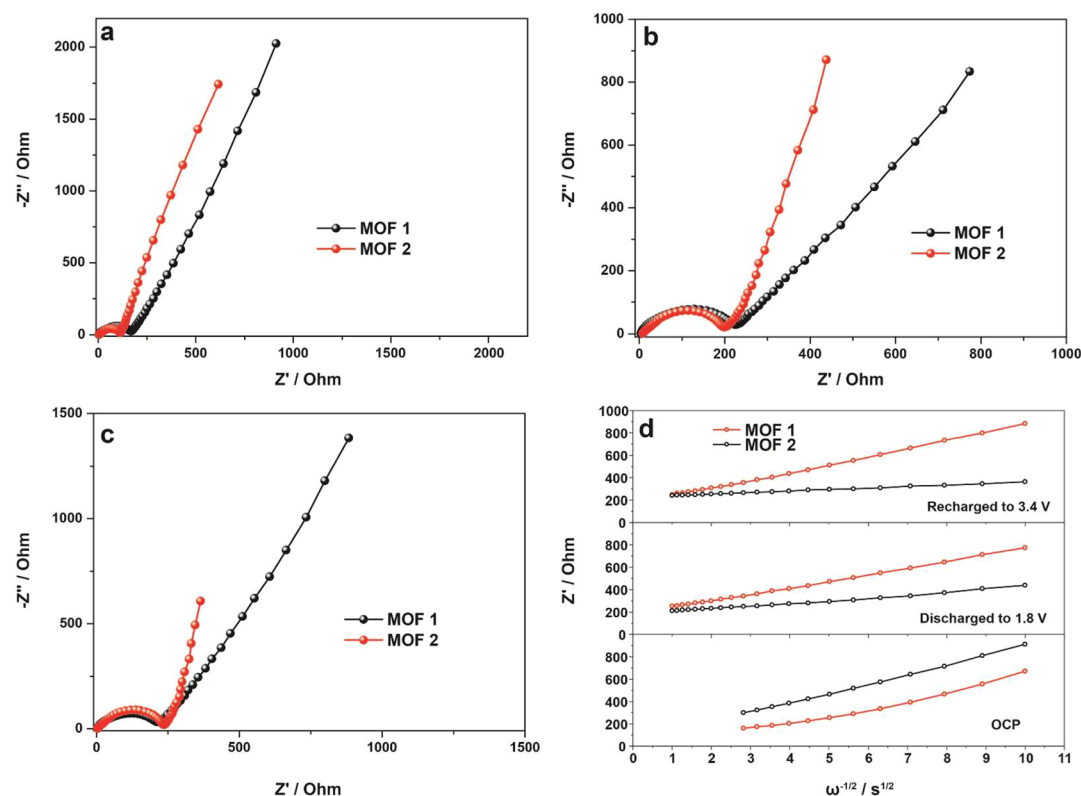
**Figure 6.** EIS (Nyquist plots) spectra of Cd(II) MOFs (MOFs **1** and **2**) at the stages of (a) open circuit potential (OCP), (b) discharged to 1.8 V, and (c) recharged to 3.4 V after potential stabilization. (d) Relationship between real impedance ($Z'$) and radial frequency ($\omega^{-1/2}$) at the different stabilization states.

observed in the potential range of 2.6−2.3 V but also delivers a plateau capacity of ∼40 mA h g$^{-1}$. The two Cd(II) MOFs present specific capacities of 42.1 and 46.8 mA h g$^{-1}$ during the initial discharge with capacity retention ratios of 77.2 and 78.4%, respectively, even after 50 cycles (Figure 4a,b,f). However, although the Co(II) MOFs (MOFs **3** and **4**) provide higher initial experimental specific capacities (45.9 and 62.7 mA h g$^{-1}$, respectively), they all give poor cycling performances because of their unstable structure during the electrochemical process compared with that of Cd(II) MOFs, as confirmed by XRD results depicted in Figure S18.

The cyclic voltammograms (CVs) of the four MOFs and DPNDI ligand (Figure 5 and Figure S15) are consistent with the galvanostatic discharge−charge results. The CVs of MOF **1** (Figure 5a) show one pair of broad redox peaks due to the poor kinetic properties of the 1D chain structure. However, in the case of MOF **2**, which is constructed from the same Cd(II) node, two sharp cathodic peaks around 2.41 and 2.34 V are observed, corresponding to the two-step lithiation process of MOF **2**. In the first delithiation process, three sharp anodic peaks (located at 2.37, 2.46, and 2.80 V) and one broad anodic peak (centered at 2.63 V) are observed, indicating four electrochemical active sites participated in this oxidation process. However, from the CV data (integration of anodic parts, 147 C g$^{-1}$) and charge capacity (47.5 mA h g$^{-1}$) of the electrodes, only two electrons (and two Li$^+$ ions) per molecule unit are extracted from the lithiated electrode during the delithiation process. This result is consistent with previous work on NDI, whereby a two-electron reaction occurs, although it has four active sites for one molecule unit.[48] However, after the first CV, the peak at 2.80 V disappears

because of the irreversible process of the electrode in this potential range. Similar irreversible reaction was also observed in Co(II) MOFs (MOFs **3** and **4**) and the DPNDI ligand as shown in the CV plots (Figure S15).

To understand the electronic and ionic transport kinetics that determine the electrochemical performance, the electrochemical impedance spectra of the Cd(II) MOF (MOFs **1** and **2**) electrodes at the stages of open circuit potential (OCP), discharge, and charge in the first lithiation−delithiation cycle are studied as shown in Figure 6. From the EIS curves of MOF **1** and **2** electrodes at OCP (Figure 6a), a smaller semicircle of the MOF **2** cell demonstrates that 2D MOF **2** has an electrode conductivity better than that of 1D MOF **1**.[51] Moreover, the semicircle of the MOF **2** electrode increased with further discharge−charge cycling (Figure S16), demonstrating that the charge transfer resistance of the MOF **2** cell increases continuously during the electrochemical cycling process.

To obtain the diffusion coefficient for diffusion of lithium ions ($D_{Li}$) into the MOF electrodes, the low-frequency region related to Warburg impedance ($Z_W$) was selected for analysis. The $D_{Li}$ can be deduced from the $Z_W$, as follows:

$$Z_W = \sigma_W(1 - j)\omega^{-1/2} \tag{1}$$

where $\omega$ is the radial frequency and $\sigma_W$ is the Warburg impedance coefficient, which is determined from the real impedance ($Z'$) plotted versus the radial frequency ($\omega^{-1/2}$), as shown in Figure 6d. The $D_{Li}$ is then given by[51−57]

$$D_{Li} = 0.5\left(\frac{RT}{AF^2\sigma W^C}\right)^2 = 4.52 \times 10^{-13}\left(\frac{1}{\sigma W^C}\right)^2 \tag{2}$$
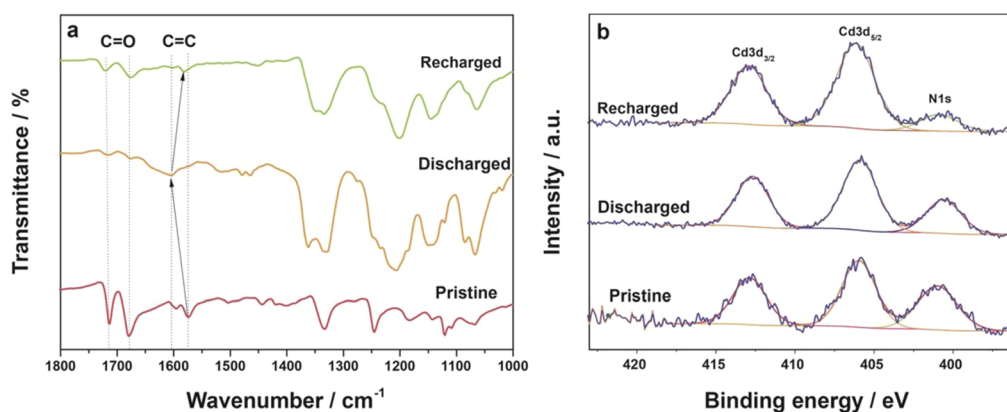
**Figure 7.** (a) FTIR spectra and (b) XP Cd 3d core levels of the MOF **2** electrodes at the stages of pristine, discharged (to 1.8 V), and recharged (to 3.4 V).

where $T$ is the absolute temperature, $R$ is the gas constant, $C$ is the molar concentration of Li$^+$ ions (moles per cubic centimeter), $A$ is the geometric electrode area (1.54 cm$^2$), and $F$ is the Faraday constant. Equation 2 is valid only when semi-infinite diffusion conditions are fulfilled. The values of $\sigma_W$, $C$, and $D_{Li}$ at various potentials are listed in Table S1. At the discharged state (1.8 V), MOF **2** shows a lithium-ion diffusion coefficient ($D_{Li} = 4.21 \times 10^{-14}$ cm$^2$ s$^{-1}$) 5-fold larger than that for MOF **1** ($8.80 \times 10^{-15}$ cm$^2$ s$^{-1}$), indicating superior kinetic properties of 2D porous Cd(II) MOFs compared to those of 1D nonporous Cd(II) MOFs in LIBs.

The redox mechanism of the various synthesized MOFs with lithium ion is studied using FTIR and XPS analysis during the lithiation−delithiation process (Figure 7 and Figures S19−S21). The MOF cells were disassembled in a glovebox at the discharged (1.8 V) and recharged (3.4 V) states to prepare test samples. Pristine MOF **2** displays absorbance signals at 1684 and 1717 cm$^{-1}$ that can be assigned to redox active C=O bonds, which show the variation in intensity during the charge−discharge process. The signal intensity of C=O bonds decreases during discharge and increases during recharge, suggesting partial lithiation of carbonyl groups. The absorbance signal assigned to vibration of C=C bonds shifts from 1578 to 1607 cm$^{-1}$, indicating the formation of new C=C bonds in the discharged state. After recharge to 3.4 V, the peak at 1607 cm$^{-1}$ returns to 1580 cm$^{-1}$, which is close to that of the original MOF **2**, implying a reversible lithiation and delithiation process. The reversible changes in the C=O and C=C bond vibrational modes coincide with the lithiation and delithiation of MOF **2** on the organic linkers (DPNDI), which confirms the participation of C=O bonds in the electrochemical redox reaction. The XPS Cd 3d core levels of the MOF **2** electrodes did not change their peak position or profile throughout the stages of discharged (1.8 V) and recharged (3.4 V) states, indicating that the metal centers (Cd$^{2+}$) did not undergo redox reactions during the electrochemical process. XPS analysis also confirms the Co(II) ion remains intact in MOF **4** electrodes during the lithiation−delithiation process (Figure S21). These results prove that only the organic linkers DPNDI take part in the electrochemical process instead of metal ions, which is quite unusual compared to the previously reported case for MOF electrodes for LIBs.[43,45,47]

## 4. CONCLUSIONS

In conclusion, two pairs of isostructural naphthalenediimide-based MOFs with different porosities are synthesized via anion and thermodynamic control. These MOFs are employed as cathode materials for lithium-ion batteries. Their structure-dependent electrochemical performances are investigated. The electrochemical stability and reversibility of the MOF electrodes are strongly influenced by metal nodes in the MOFs. As shown here, the Cd(II) MOFs (MOFs **1** and **2**) exhibit a capacity higher than and a cycling stability better than those of Co(II) MOFs (MOFs **3** and **4**). Besides the metal nodes, the electrochemical properties are also influenced by porosity. Because of the large porosity of 2D MOF **2**, it allows a lithium-ion diffusion coefficient ($D_{Li}$) that is much higher than that of 1D nonporous MOF **1**. Although the gravimetric specific capacity of these MOFs is not very high (only 47 mA h g$^{-1}$) because of the high molecular weight and limited number of inserted Li atoms per formula unit, our work indicates that the proper design of functionalities will improve the ion storage capacity of these materials.

## ■ ASSOCIATED CONTENT

### Ⓢ Supporting Information
The Supporting Information is available free of charge on the ACS Publications website at DOI: 10.1021/acsami.6b11772.

> Crystal information; SEM and TEM images; XRD patterns; XPS spectra; FTIR spectra; TGA; CVs, charge−discharge curves, and cycling performance; and a digital picture of electrodes (PDF)

## ■ AUTHOR INFORMATION
### Corresponding Author
*E-mail: chmlohkp@nus.edu.sg. Telephone: (65) 6516 2658. Fax: (65) 6779 1691.
### Author Contributions
B.T., G.-H.N., and Q.G. contributed equally to this work.
### Notes
The authors declare no competing financial interest.

## ■ ACKNOWLEDGMENTS

## ■ REFERENCES

(1) Padhi, A. K.; Nanjundaswamy, K. S.; Goodenough, J. B. Phospho-Olivines as Positive-Electrode Materials for Rechargeable Lithium Batteries. *J. Electrochem. Soc.* **1997**, *144*, 1188−1194.

(2) Tarascon, J.-M.; Armand, M. Issues and Challenges Facing Rechargeable Lithium Batteries. *Nature* **2001**, *414*, 359−367.

(3) Armand, M.; Tarascon, J.-M. Building Better Batteries. *Nature* **2008**, *451*, 652−657.

(4) Bruce, P. G.; Scrosati, B.; Tarascon, J.-M. Nanomaterials for Rechargeable Lithium Batteries. *Angew. Chem., Int. Ed.* **2008**, *47*, 2930−2946.

(5) Armand, M.; Grugeon, S.; Vezin, H.; Laruelle, S.; Ribiere, P.; Poizot, P.; Tarascon, J.-M. Conjugated Dicarboxylate Anodes for Li-ion Batteries. *Nat. Mater.* **2009**, *8*, 120−125.

(6) Lee, S. W.; Yabuuchi, N.; Gallant, B. M.; Chen, S.; Kim, B. S.; Hammond, P. T.; Shao-Horn, Y. High-power Lithium Batteries from Functionalized Carbon-nanotube Electrodes. *Nat. Nanotechnol.* **2010**, *5*, 531−537.

(7) Bruce, P. G.; Freunberger, S. A.; Hardwick, L. J.; Tarascon, J.-M. Li-$O_2$ and Li-S Batteries with High Energy Storage. *Nat. Mater.* **2011**, *11*, 19−29.

(8) Choi, N. S.; Chen, Z.; Freunberger, S. A.; Ji, X.; Sun, Y. K.; Amine, K.; Yushin, G.; Nazar, L. F.; Cho, J.; Bruce, P. G. Challenges Facing Lithium Batteries and Electrical Double-Layer Capacitors. *Angew. Chem., Int. Ed.* **2012**, *51*, 9994−10024.

(9) Mizushima, K.; Jones, P. C.; Wiseman, P. J.; Goodenough, J. B. $Li_xCoO_2$ ($0 < x \leq 1$): A New Cathode Material for Batteries of High Energy Density. *Mater. Res. Bull.* **1980**, *15*, 783−789.

(10) Xu, B.; Qian, D.; Wang, Z.; Meng, Y. S. Recent Progress in Cathode Materials Research for Advanced Lithium Ion Batteries. *Mater. Sci. Eng., R* **2012**, *73*, 51−65.

(11) Ohzuku, T.; Ueda, A.; Nagayama, M.; Iwakoshi, Y.; Komori, H. Comparative Study of $LiCoO_2$, $LiNi_{12}Co_{12}O_2$ and $LiNiO_2$ for 4 V Secondary Lithium Cells. *Electrochim. Acta* **1993**, *38*, 1159−1167.

(12) Tarascon, J.-M.; Guyomard, D. The $Li_{1+x}Mn_2O_4$/C Rocking-Chair System: A Review. *Electrochim. Acta* **1993**, *38*, 1221−1231.

(13) Xia, Y. Y.; Yoshio, M. An Investigation of Lithium Ion Insertion into Spinel Structure Li-Mn-O Compounds. *J. Electrochem. Soc.* **1996**, *143*, 825−833.

(14) Ceder, G.; Chiang, Y.-M.; Sadoway, D. R.; Aydinol, M. K.; Jang, Y. I.; Huang, B. Identification of Cathode Materials for Lithium Batteries Guided by First-Principles Calculations. *Nature* **1998**, *392*, 694−696.

(15) Croce, F.; D'Epifanio, A.; Hassoun, J.; Deptula, A.; Olczac, T.; Scrosati, B. A Novel Concept for the Synthesis of an Improved $LiFePO_4$ Lithium Battery Cathode. *Electrochem. Solid-State Lett.* **2002**, *5*, A47−A50.

(16) Whittingham, M. S. Lithium Batteries and Cathode Materials. *Chem. Rev.* **2004**, *104*, 4271−4301.

(17) Zhou, L.; Zhao, D.; Lou, X. W. $LiNi_{0.5}Mn_{1.5}O_4$ Hollow Structures as High-Performance Cathodes for Lithium-Ion Batteries. *Angew. Chem., Int. Ed.* **2012**, *51*, 239−241.

(18) Zhang, L.; Xiang, H.; Li, Z.; Wang, H. Porous $Li_3V_2(PO_4)_3$/C Cathode with Extremely High-Rate Capacity Prepared by a Sol-Gel-Combustion Method for Fast Charging and Discharging. *J. Power Sources* **2012**, *203*, 121−125.

(19) Xu, G.-L.; Wang, Q.; Fang, J.-C.; Xu, Y.-F.; Li, J.-T.; Huang, L.; Sun, S.-G. Tuning the Structure and Property of Nanostructured Cathode Materials of Lithium Ion and Lithium Sulfur Batteries. *J. Mater. Chem. A* **2014**, *2*, 19941−19962.

(20) Tian, B.; Ning, G.-H.; Tang, W.; Peng, C.; Yu, D.; Chen, Z.; Xiao, Y.; Su, C.; Loh, K. P. Polyquinoneimines for Lithium Storage: More Than the Sum of Its Parts. *Mater. Horiz.* **2016**, *3*, 429−433.

(21) Poizot, P.; Dolhem, F. Clean Energy New Deal for a Sustainable World: from Non-$CO_2$ Generating Energy Sources to Greener Electrochemical Storage Devices. *Energy Environ. Sci.* **2011**, *4*, 2003−2019.

(22) Liang, Y.; Tao, Z.; Chen, J. Organic Electrode Materials for Rechargeable Lithium Batteries. *Adv. Energy Mater.* **2012**, *2*, 742−769.

(23) Song, Z.; Zhou, H. Towards Sustainable and Versatile Energy Storage Devices: An Overview of Organic Electrode Materials. *Energy Environ. Sci.* **2013**, *6*, 2280−2301.

(24) Häupler, B.; Wild, A.; Schubert, U. S. Carbonyls: Powerful Organic Materials for Secondary Batteries. *Adv. Energy Mater.* **2015**, *5*, 1402034.

(25) Kitagawa, S.; Kitaura, R.; Noro, S. Functional Porous Coordination Polymers. *Angew. Chem., Int. Ed.* **2004**, *43*, 2334−2375.

(26) Ferey, G. Hybrid Porous Solids: Past, Present, Future. *Chem. Soc. Rev.* **2008**, *37*, 191−214.

(27) Yaghi, O. M.; O'Keeffe, M.; Ockwig, N. W.; Chae, H. K.; Eddaoudi, M.; Kim, J. Reticular Synthesis and the Design of New Materials. *Nature* **2003**, *423*, 705−714.

(28) Li, J.-R.; Kuppler, R. J.; Zhou, H.-C. Selective Gas Adsorption and Separation in Metal-Organic Frameworks. *Chem. Soc. Rev.* **2009**, *38*, 1477−1504.

(29) Czaja, A. U.; Trukhan, N.; Mueller, U. Industrial Applications of Metal-Organic Frameworks. *Chem. Soc. Rev.* **2009**, *38*, 1284−1293.

(30) Murray, L. J.; Dincă, M.; Long, J. R. Hydrogen Storage in Metal-Organic Frameworks. *Chem. Soc. Rev.* **2009**, *38*, 1294−1314.

(31) Lee, J. Y.; Farha, O. K.; Roberts, J.; Scheidt, K. A.; Nguyen, S. T.; Hupp, J. T. Metal-Organic Framework Materials as Catalysts. *Chem. Soc. Rev.* **2009**, *38*, 1450−1459.

(32) Ma, L.; Abney, C.; Lin, W. Enantioselective Catalysis with Homochiral Metal-Organic Frameworks. *Chem. Soc. Rev.* **2009**, *38*, 1248−1256.

(33) Corma, A.; Garcia, H.; Llabrés i Xamena, F. X. Engineering Metal Organic Frameworks for Heterogeneous Catalysis. *Chem. Rev.* **2010**, *110*, 4606−4655.

(34) Yoon, M.; Srirambalaji, R.; Kim, K. Homochiral Metal-Organic Frameworks for Asymmetric Heterogeneous Catalysis. *Chem. Rev.* **2012**, *112*, 1196−1231.

(35) Inokuma, Y.; Yoshioka, S.; Ariyoshi, J.; Arai, T.; Hitora, Y.; Takada, K.; Matsunaga, S.; Rissanen, K.; Fujita, M. X-ray Analysis on the Nanogram to Microgram Scale Using Porous Complexes. *Nature* **2013**, *495*, 461−466.

(36) Inokuma, Y.; Ning, G.-H.; Fujita, M. Reagent-installed Capsule Network: Selective Thiocarbamoylation of Aromatic Amines in Crystals with Preinstalled $CH_3NCS$. *Angew. Chem., Int. Ed.* **2012**, *51*, 2379−2381.

(37) Ning, G.-H.; Inokuma, Y.; Fujita, M. Stable Encapsulation of Acrylate Esters in Networked Molecular Capsules. *Chem. - Asian J.* **2014**, *9*, 466−468.

(38) Chen, B.; Xiang, S.; Qian, G. Metal-Organic Frameworks with Functional Pores for Recognition of Small Molecules. *Acc. Chem. Res.* **2010**, *43*, 1115−1124.

(39) Ning, G.-H.; Matsumura, K.; Inokuma, Y.; Fujita, M. A Saccharide-Based Crystalline Sponge for Hydrophilic Guests. *Chem. Commun.* **2016**, *52*, 7013−7015.

(40) Allendorf, M. D.; Bauer, C. A.; Bhakta, R. K.; Houk, R. J. T. Luminescent Metal-Organic Frameworks. *Chem. Soc. Rev.* **2009**, *38*, 1330−1352.

(41) Cui, Y.; Yue, Y.; Qian, G.; Chen, B. Luminescent Functional Metal-Organic Frameworks. *Chem. Rev.* **2012**, *112*, 1126−1162.

(42) Li, X.; Cheng, F.; Zhang, S.; Chen, J. Shape-Controlled Synthesis and Lithium-storage Study of Metal-Organic Frameworks $Zn_4O(1,3,5-benzenetribenzoate)_2$. *J. Power Sources* **2006**, *160*, 542−547.

(43) Feŕey, G.; Millange, F.; Morcrette, M.; Serre, C.; Doublet, M. L.; Grenèche, J. M.; Tarascon, J.-M. Mixed-Valence Li/Fe-Based Metal-

Organic Frameworks with Both Reversible Redox and Sorption Properties. *Angew. Chem., Int. Ed.* **2007**, *46*, 3259−3263.

(44) Nagarathinam, M.; Saravanan, K.; Phua, E. J. H.; Reddy, M. V.; Chowdari, B. V. R.; Vittal, J. J. Redox-Active Metal-Centered Oxalato Phosphate Open Framework Cathode Materials for Lithium Ion Batteries. *Angew. Chem., Int. Ed.* **2012**, *51*, 5866−5870.

(45) de Combarieu, G.; Morcrette, M.; Millange, F.; Guillou, N.; Cabana, J.; Grey, C. P.; Margiolaki, I.; Feŕey, G.; Tarascon, J.-M. Influence of the Benzoquinone Sorption on the Structure and Electrochemical Performance of the MIL-53(Fe) Hybrid Porous Material in a Lithium-Ion Battery. *Chem. Mater.* **2009**, *21*, 1602−1611.

(46) Nguyen, T. L. A.; Demir-Cakan, R.; Devic, T.; Morcrette, M.; Ahnfeldt, T.; Auban-Senzier, P.; Stock, N.; Goncalves, A.-M.; Filinchuk, Y.; Tarascon, J.-M.; Feŕey, G. 3-D Coordination Polymers Based on the Tetrathiafulvalenetetracarboxylate (TTF-TC) Derivative: Synthesis, Characterization, and Oxidation Issues. *Inorg. Chem.* **2010**, *49*, 7135−7143.

(47) Zhang, Z.; Yoshikawa, H.; Awaga, K. Monitoring the Solid-State Electrochemistry of Cu(2,7-AQDC) (AQDC = Anthraquinone Dicarboxylate) in a Lithium Battery: Coexistence of Metal and Ligand Redox Activities in a Metal−Organic Framework. *J. Am. Chem. Soc.* **2014**, *136*, 16112−16115.

(48) Dinolfo, P. H.; Williams, M. E.; Stern, C. L.; Hupp, J. T. Rhenium-Based Molecular Rectangles as Frameworks for Ligand-Centered Mixed Valency and Optical Electron Transfer. *J. Am. Chem. Soc.* **2004**, *126*, 12989−13001.

(49) Sheldrick, G. M. Crystal Structure Refinement with SHELXL. *Acta Crystallogr., Sect. A: Found. Adv.* **2015**, *71*, 3−8.

(50) Spek, A. L. PLATON, An Integrated Tool for the Analysis of the Results of a Single Crystal Structure Determination. *Acta Crystallogr., Sect. A: Found. Adv.* **1990**, *A46*, C34.

(51) You, Y.; Wu, X.-L.; Yin, Y.-X.; Guo, Y.-G. High-Quality Prussian Blue Crystals as Superior Cathode Materials for Room-Temperature Sodium-Ion Batteries. *Energy Environ. Sci.* **2014**, *7*, 1643−1647.

(52) Tian, B.; Światowska, J.; Maurice, V.; Pereira-Nabais, C.; Seyeux, A.; Marcus, P. Insight into Lithium Diffusion in Conversion-Type Iron Oxide Negative Electrode. *J. Phys. Chem. C* **2015**, *119*, 919−925.

(53) Tian, B.; Światowska, J.; Maurice, V.; Zanna, S.; Seyeux, A.; Klein, L. H.; Marcus, P. Combined Surface and Electrochemical Study of the Lithiation/Delithiation Mechanism of the Iron Oxide Thin-Film Anode for Lithium-Ion Batteries. *J. Phys. Chem. C* **2013**, *117*, 21651−21661.

(54) Tian, B.; Xiang, H.; Zhang, L.; Li, Z.; Wang, H. Niobium Doped Lithium Titanate as a High Rate Anode Material for Li-ion Batteries. *Electrochim. Acta* **2010**, *55*, 5453−5458.

(55) Li, X.; Qu, M. Z.; Yu, Z. L. Structural and Electrochemical Performances of $Li_4Ti_{5-x}Zr_xO_{12}$ as Anode Material for Lithium-Ion Batteries. *J. Alloys Compd.* **2009**, *487*, L12−L17.

(56) Shenouda, A. Y.; Liu, H. K. Electrochemical Behaviour of Tin Borophosphate Negative Electrodes for Energy Storage Systems. *J. Power Sources* **2008**, *185*, 1386−1391.

(57) Peng, Z.; Yi, X.; Liu, Z.; Shang, J.; Wang, D. Triphenylamine-Based Metal-Organic Frameworks as Cathode Materials in Lithium-Ion Batteries with Coexistence of Redox Active Sites, High Working Voltage, and High Rate Stability. *ACS Appl. Mater. Interfaces* **2016**, *8*, 14578−14585.